RESEARCH PAPER PRESENTED AT ANADE 2013 ADVANCES IN NUMERICAL AND ANALYTICAL TOOLS FOR DETACHED FLOW PREDICTION

Direct and adjoint global stability analysis of turbulent transonic flows over a NACA0012 profile

M. C. Iorio[1], L. M. González[2,*,†] and E. Ferrer[3]

SUMMARY

In this work, various turbulent solutions of the two-dimensional (2D) and three-dimensional compressible Reynolds averaged Navier–Stokes equations are analyzed using global stability theory. This analysis is motivated by the onset of flow unsteadiness (Hopf bifurcation) for transonic buffet conditions where moderately high Reynolds numbers and compressible effects must be considered. The buffet phenomenon involves a complex interaction between the separated flow and a shock wave. The efficient numerical methodology presented in this paper predicts the critical parameters, namely, the angle of attack and Mach and Reynolds numbers beyond which the onset of flow unsteadiness appears. The geometry, a NACA0012 profile, and flow parameters selected reproduce situations of practical interest for aeronautical applications.

The numerical computation is performed in three steps. First, a steady baseflow solution is obtained; second, the Jacobian matrix for the RANS equations based on a finite volume discretization is computed; and finally, the generalized eigenvalue problem is derived when the baseflow is linearly perturbed. The methodology is validated predicting the 2D Hopf bifurcation for a circular cylinder under laminar flow condition. This benchmark shows good agreement with the previous published computations and experimental data.

In the transonic buffet case, the baseflow is computed using the Spalart–Allmaras turbulence model and represents a mean flow where the high frequency content and length scales of the order of the shear-layer thickness have been averaged. The lower frequency content is assumed to be decoupled from the high frequencies, thus allowing a stability analysis to be performed on the low frequency range. In addition, results of the corresponding adjoint problem and the sensitivity map are provided for the first time for the buffet problem. Finally, an extruded three-dimensional geometry of the NACA0012 airfoil, where all velocity components are considered, was also analyzed as a Triglobal stability case, and the outcoming results were compared to the previous 2D limited model, confirming that the buffet onset is well detected.

KEY WORDS: stability analysis; shock wave; RANS turbulence model; buffet; adjoint mode; structural sensitivity

1. INTRODUCTION

Flow unsteadiness is commonly seen as an important problem in engineering applications, specially because it could produce undesirable load variations leading to structural instabilities. For this reason, the determination of the origin of such instabilities results crucial to assure a better understanding and relief of such phenomenon.

*Correspondence to: L. M. González, Universidad Politécnica de Madrid, Avda. Arco del Triunfo 4 28004 Madrid Spain.
†E-mail: leo.gonzalez@upm.es

One of the most challenging instability problems is provided by the transonic buffet phenomenon. In transonic conditions, a strong interaction between the shock wave and the boundary layer leads to an oscillation of the shock location and consequently of the lift aerodynamic forces. This unsteady behavior could generate damaging structure vibrations called buffeting. The studies on the phenomenon started during the 1930s, when a monoplane Junkers F13 crashed because of tail buffeting, killing all passengers [1]. Nowadays, the design standard for airplanes inherently restrict the buffeting intensity, defining the buffet onset as a pilot seat acceleration of +/- 0.2 g that requires 30% margin for the cruise lift coefficient (+/- 0.05 g for business jets), therefore limiting the airplane envelope, this clearly highlights the need to evaluate the origin of the phenomenon and calculate the aerodynamic buffet onset.

The first experiments on this subject were conducted on a NACA0012 airfoil by McDevitt and Okuno [2]. They showed the appearance of pressure fluctuations downstream of the shock once the critical angle of attack was reached, therefore determining the onset of unsteadiness when the Mach number is kept constant and the angle of attack is increased.

Some empirical criteria for the buffet identification were presented by Lee [3]. This work described and explained the flow behavior but was not accurate in predicting the onset of buffet.

From the numerical point of view, unsteady CFD simulations were used by Drikakis [4] and Chung *et al.* [5] to identify the critical buffet angle for the experimental setup of McDevitt and Okuno. Another complete analysis was carried out by Brunet *et al.* [6] on the ONERA supercritical airfoil OAT15A. They compared wind tunnel experimental results with unsteady RANS and detached Eddy simulations computations and characterized the phenomenon for various angles of attack. Despite the relative success of this type of approaches, these computations are found to be computationally intensive and difficult to analyze in detail, which justifies the exploration of alternative methods such as linear stability analysis.

Global stability theory is a useful technique when determining the instability onset. In fact, Theofilis [7] explains how this theory is successful in multiple aeronautical applications. The application of this theory to the buffet onset analysis on the NACA0012 airfoil was performed for the first time by Crouch [8, 9]. He found remarkably good agreement between the global stability analysis results and the experiments of McDevitt and Okuno, providing a valuable connection between the transonic buffet onset and a linear global instability. Moreover, these ideas were further extended to more complex 3D flows by Crouch [10] for a quasi 3D analysis of the vortex shedding phenomenon behind a 3D wavy circular cylinder with variable spanwise diameter. The author provided the final global response, coupling the two-dimensional (2D) analysis of different geometry planes with the Ginzburg–Landau equation. It is also worth mentioning the contribution of Timme *et al.* [11] where an inexact Lyapunov inverse iteration method for the analysis of aeroelastic and fluid stability problems was developed.

The main objectives of this work follow. First, we show the flexibility and usability of the global instability analysis to predict the buffet onset. In our method, and contrary to previous works, the Navier–Stokes equations are first discretized and subsequently linearized to obtain the global stability formulation. This methodology is general and can be used for complex problems and where turbulent effects and shock waves have non-negligible effects in determining flow unsteadiness. Second, for future attempts in controlling or alleviating the buffeting phenomenon, we extend the linear global stability analysis to provide adjoint modes. The combination of direct and adjoint modes enables the detection of the maximum structural sensitivity area, which is provided for the first time (to the authors knowledge) under transonic buffet conditions. We finally confirm that buffet effects in a three-dimensional (3D) NACA0012 wing (i.e., extruded geometry) are similar to the 2D physical phenomenon, which suggests that 2D simulations are enough to capture the relevant physics.

2. MATHEMATICAL MODEL

The cases included in this work are characterized by transonic and turbulent effects, for this reason, the mathematical description of the problem is given by the compressible version of the Reynolds averaged Navier–Stokes equations. The turbulent scales are modeled using the Spalart–Allmaras

(S–A) turbulence model [12] taking into account a compressibility correction [13], see details in the Appendix. This set of equations can be written in conservative form as

$$\frac{\partial}{\partial t}\int_{\Omega}\mathbf{q}d\,\Omega = -\int_{\partial\Omega}\bar{\bar{\mathbf{F}}}\cdot\mathbf{n}dS, \tag{1}$$

with the vector of unknowns defined as

$$\mathbf{q} = \begin{pmatrix} \rho \\ \rho u \\ \rho v \\ \rho w \\ \rho E \\ \rho\tilde{\nu} \end{pmatrix}, \tag{2}$$

where Ω is the entire flow domain control volume that has boundaries $\partial\Omega$ with outer normal $\mathbf{n}$. In addition, ρ is the fluid density, (u, v, w) denote the velocity components, $\tilde{\nu}$ is the turbulent kinematic viscosity, and $E = C_vT + (u^2 + v^2 + w^2)/2$ is the total specific energy. The product of the specific heat capacity of the gas at constant volume C_v and the temperature T represents the thermal specific energy, and $H = C_pT$ is the specific enthalpy. The specific heat capacities of the gas at constant volume C_v and pressure C_p are both assumed constant, consequently, we can also define the constant adiabatic coefficient $\gamma = C_p/C_v$. Because a finite volume [14] approach is selected for spatial discretization, the change of the flow conditions in a control volume Ω is given by the normal component of the flux through the control volume boundary $\partial\Omega$. The flux density tensor $\bar{\bar{\mathbf{F}}}$ can be decomposed along the three cartesian coordinate directions such that

$$\bar{\bar{\mathbf{F}}} = \mathbf{F}\vec{e}_x + \mathbf{G}\vec{e}_y + \mathbf{H}\vec{e}_z, \tag{3}$$

with inviscid and viscous fluxes, denoted with indices i and v, respectively.

$$\mathbf{F} = \mathbf{F}_i + \mathbf{F}_v = \begin{pmatrix} \rho u \\ \rho u^2 + p \\ \rho uv \\ \rho uw \\ \rho Hu \end{pmatrix} - \begin{pmatrix} 0 \\ \tau_{xx} \\ \tau_{xy} \\ \tau_{xz} \\ u\tau_{xx} + v\tau_{xy} + w\tau_{xz} + k_{eff}\frac{\partial T}{\partial x} \end{pmatrix}, \tag{4}$$

$$\mathbf{G} = \mathbf{G}_i + \mathbf{G}_v = \begin{pmatrix} \rho v \\ \rho uv \\ \rho v^2 + p \\ \rho vw \\ \rho Hv \end{pmatrix} - \begin{pmatrix} 0 \\ \tau_{xy} \\ \tau_{yy} \\ \tau_{yz} \\ u\tau_{xy} + v\tau_{yy} + w\tau_{yz} + k_{eff}\frac{\partial T}{\partial y} \end{pmatrix}, \tag{5}$$

$$\mathbf{H} = \mathbf{H}_i + \mathbf{H}_v = \begin{pmatrix} \rho w \\ \rho uw \\ \rho vw \\ \rho w^2 + p \\ \rho Hw \end{pmatrix} - \begin{pmatrix} 0 \\ \tau_{xz} \\ \tau_{yz} \\ \tau_{zz} \\ u\tau_{xz} + v\tau_{yz} + w\tau_{zz} + k_{eff}\frac{\partial T}{\partial z} \end{pmatrix}. \tag{6}$$

Here, p is the fluid pressure and τ_{sj} is the effective stress tensor, which can be defined by its components

$$\tau_{sj} = 2\mu_{eff}\frac{\partial u_s}{\partial x_j} - \frac{2}{3}\mu_{eff}\frac{\partial u_k}{\partial x_k}. \tag{7}$$

The effective dynamic viscosity μ_{eff} and effective heat conductivity k_{eff} are defined as

$$\mu_{eff} = \mu_l + \rho\nu_t \quad , \qquad k_{eff} = \frac{\gamma}{\gamma - 1}\left(\frac{\mu_l}{Pr} + \frac{\rho\nu_t}{Pr_t}\right), \tag{8}$$

where μ_l is the local laminar viscosity, and Pr and Pr_t are the Prandtl number and the turbulent Prandtl number, respectively. The turbulent kinematic viscosity ν_t is calculated using the SŰA turbulence model [12]. The S–A turbulence model is a one equation model with a transport equation directly formulated for the eddy viscosity, further details are provided in the Appendix.

Subsequently, the pressure may be calculated as

$$p = (\gamma - 1)\rho\left(E - \frac{u^2 + v^2 + w^2}{2}\right). \tag{9}$$

From Equation (1) and for a control volume fixed in time and space, the temporal change of the conservative variables $\mathbf{q}$ can be derived as

$$\frac{\partial \mathbf{q}}{\partial t} = -\frac{1}{|\Omega|}\int_{\partial\Omega} \bar{\bar{\mathbf{F}}} \cdot \mathbf{n} dS = -\frac{1}{|\Omega|}\mathbf{U}^F, \tag{10}$$

where $\mathbf{U}^F$ represents the fluxes over the boundaries of the control volume Ω. The flow domain Ω is discretized, using a dual mesh into a finite number of subdomains Ω_i, where each subdomain contains $\mathcal{N}$ faces.

To solve the problem, the temporal variation of the flow quantities can be written in general form for a subdomain i as

$$\frac{\partial \mathbf{q}_i}{\partial t} + \frac{1}{|\Omega_i|}\sum_{j=1}^{\mathcal{N}} \mathbf{U}_j^F = \mathbf{0}. \tag{11}$$

In the steady-state case, the problem is solved using a fictitious pseudo-time τ (instead of t) and marching in time until its steady-state solution is reached. The pseudo-time integration is performed either utilizing the low-storage K-step Runge–Kutta scheme or using a backward Euler implicit scheme. The linear system is solved using a Lower-Upper Symmetric Gauss Seidel Method (LU-SGS) method with the Jacobians approximated by a first-order scheme [15]. To accelerate and improve convergence, typical numerical techniques such as local time stepping, residual smoothing, and multigrid methods may be used. Equation (11) becomes

$$\Omega_i \frac{\partial \mathbf{Q}_i}{\partial \tau} + \mathbf{R}_i = \mathbf{0} \quad , \qquad \mathbf{R}_i = \sum_{j=1}^{\mathcal{N}} \mathbf{U}_j^F, \tag{12}$$

where $\mathbf{R}_i$ is the residual and $\mathbf{Q}_i$ represents a particular steady solution of the problem for the subdomain i. Vectors $\mathbf{Q}_i$ and $\mathbf{R}_i$ have dimensions that depend on the number of fluid variables N_b considered. Namely, N_b =4, 5, or 6 depending whether a 2D laminar case, a 2D turbulent case, or a 3D turbulent case is studied, respectively.

The boundary conditions on the body surface are as follows:

$$u = v = w = 0 \qquad \tilde{\nu} = 0 \qquad \frac{\partial T}{\partial \mathbf{n}} = \frac{\partial \rho}{\partial \mathbf{n}} = 0 \tag{13}$$

where n is the normal direction to the body surface. For external boundaries, a far-field boundary condition is used. For lateral boundaries in 3D cases, a symmetry boundary condition is used.

The convective fluxes crossing the far-field boundary faces are calculated using the AUSM Riemann solver [14], and the flow conditions outside the boundary faces are determined employing

Whitfield theory [16]. Thus, the scheme used in the computational domain is hybrid, because it has the robustness of the van Leer scheme near the shock and the low diffusive properties in smooth regions of the AUSM scheme.

It should be noted that the common practice when performing stability analysis is to start by linearizing the continuous equations, which are subsequently discretized. However, in this work, the compressible Navier–Stokes equations are first discretized and then linearized.

3. STABILITY ANALYSIS

3.1. Direct problem

From Equation (12), the finite volume formulation can be written in compact form as

$$\mathbf{B}\frac{\partial \mathbf{q}}{\partial t} = \mathbf{R}(\mathbf{q}), \tag{14}$$

where $\mathbf{B}$ is a diagonal matrix with leading dimension $N_b N$ containing the volumes associated to each finite cell, N being the number of finite volumes contained in the domain. The dependence of the matrix $\mathbf{R}$ on the fluid variables $\mathbf{q}$ has been explicitly indicated.

The basic flow fluid variables are perturbed by small amplitude functions $\tilde{\mathbf{q}}(\mathbf{x}, t)$ as follows:

$$\mathbf{q}(\mathbf{x}, t) = \mathbf{Q}(\mathbf{x}) + \varepsilon\tilde{\mathbf{q}}(\mathbf{x}, t), \tag{15}$$

where $\varepsilon \ll 1$.

Introducing this discrete solution in expression (14) and linearizing, we obtain

$$\varepsilon\mathbf{B}\frac{\partial \tilde{\mathbf{q}}}{\partial t} = \mathbf{R}(\mathbf{Q} + \varepsilon\tilde{\mathbf{q}}) \approx \mathbf{R}(\mathbf{Q}) + \varepsilon\left[\frac{\partial \mathbf{R}}{\partial \mathbf{q}}\right]_{\mathbf{Q}}\tilde{\mathbf{q}}. \tag{16}$$

The separability of temporal and spatial derivatives in (15) permits the introduction of an explicit harmonic temporal dependence of the disturbance quantities into these equations, according to the ansatz

$$\tilde{\mathbf{q}}(\mathbf{x}, t) = \widehat{q}(\mathbf{x})e^{-i\omega t}, \tag{17}$$

where $\omega = \omega_r + i\omega_i$ is the complex eigenvalue sought and $\widehat{q}$ describes the complex mode amplitude. In particular for the 2D case, Biglobal theory for infinite spanwise length is applied, and the spanwise velocity component and all derivatives in the spanwise direction are neglected. In the 3D case, Triglobal theory is applied and all velocity component and derivatives are retained. Substitution of the ansatz given by Equation (17) into the perturbed Equation (16) results in a generalized eigenvalue problem where the baseflow fields $\mathbf{Q}$ have already been obtained by the previous steady RANS computation. Assuming that $\mathbf{Q}$ is a particular solution of the steady RANS system (i.e., $\mathbf{R}(\mathbf{Q}) = 0$), Equation (16) is thus transformed into the real generalized eigenvalue problem for the determination of ω

$$\left[\frac{\partial \mathbf{R}}{\partial \mathbf{q}}\right]_{\mathbf{Q}}\widehat{\mathbf{q}} = \omega\mathbf{B}\widehat{\mathbf{q}}, \tag{18}$$

which can also be expressed as

$$\mathbf{A}\widehat{\mathbf{q}} = \omega\mathbf{B}\widehat{\mathbf{q}}, \tag{19}$$

where the matrix $\mathbf{A} = \left[\frac{\partial \mathbf{R}}{\partial \mathbf{q}}\right]_{\mathbf{Q}}$ is the Jacobian of the system, which is computed once the steady baseflow has converged, and $\omega = \omega_r + i\omega_i$ are the complex eigenvalues of the generalized system.

This file is read by the analysis code in order to compute the spectrum and includes the boundary conditions for $\widehat{\mathbf{q}}$, which are defined as follows:

$$\widehat{u} = \widehat{v} = \widehat{w} = \widehat{\tilde{v}} = 0 \quad , \qquad \frac{\partial \widehat{\rho}}{\partial \mathbf{n}} = \frac{\partial \widehat{T}}{\partial \mathbf{n}} = 0. \tag{20}$$

The number of components of the perturbed velocity amplitude in each finite volume is 2 in the Biglobal computation $(\widehat{u}(x,y), \widehat{w}(x,y))$ and 3 in the Triglobal case $(\widehat{u}(x,y,z), \widehat{v}(x,y,z), \widehat{w}(x,y,z))$. It should also be remarked that the eddy viscosity only appears in the formulation when turbulent flows are computed and consequently removed when laminar flows are analyzed. In summary, the number of perturbed variables per cell is N_v =4 in laminar 2D Biglobal cases, N_v =5 in turbulent 2D Biglobal simulations, and N_v = 6 in turbulent 3D Triglobal flows.

The real non-symmetric operator $\mathbf{A}$ is directly computed by the TAU code and saved as an output file. The operator $\mathbf{A}$, which is represented by a $(N_v N)^2$ matrix, is read from the output file and stored in sparse format. A real diagonal operator $\mathbf{B}$, representing the volume of each element, is also extracted by TAU. The eigenvector $\widehat{\mathbf{q}}$ is an $N_v N$ vector containing the perturbed variables.

The results presented in this paper are non-dimensionalized with the typical flow scales used in compressible external flows. The reference length L_0 is equal to the characteristic length of the body (the diameter or the chord length for the cylinder and NACA airfoil, respectively), the reference temperature T_0 is equal to the temperature of the incident flow, and the reference scales for velocity, dynamic viscosity, and density are defined as

$$V_0 = M\sqrt{\gamma R T} \quad , \qquad \rho_0 = \frac{Re\mu_0}{L_0 V_0} \quad , \qquad \mu_0 = \mu(T_0), \tag{21}$$

where M is the incident Mach number, R is a universal gas constant, and Re is the Reynolds number.

It is important to note that the code TAU uses a different velocity scale when the Jacobian is computed for the stability analysis, this fact must be taken into account if results are compared with other authors and a factor $1/(\sqrt{\gamma}M)$ must multiply all elements of the matrix computed $\mathbf{A}$ to obtain the expected values.

The generalized eigenvalue problem (19) accepts real and complex conjugate solutions, which correspond to stationary ($\omega_r = 0$) or traveling ($v \neq 0$) modes, where ω_r denotes the real part of the eigenvalue ω.

From a linear stability analysis point of view, the most important (least stable or unstable) eigenvalues appear close to the real axis ($\omega_i = 0$). According to the ansatz, Equation (17), stable modes have a negative imaginary part ($\omega_i < 0$) and unstable modes have a positive imaginary part ($\omega_i > 0$). In this work, an Arnoldi algorithm [17] is utilized to compute the eigenvalues. The Arnoldi method is a subspace iteration method, the computation time of which depends on the matrix factorization time and the time needed for the iterative procedure. The latter scales linearly with the Krylov subspace dimension. As experienced in previous studies [18], only eigenvalues with large modules can be obtained by a straightforward application of the algorithm. A shift-invert transformation in the Arnoldi algorithm is required to accurately capture the region of the complex plane where the unstable eigenvalues live. Because the eigenvalues closest to the imaginary axis are sought, a simple transformation is used in order to convert the original problem into one where the desired values are close to the real axis. Note that the eigenvectors are not affected by this transformation. Specifically, defining $\mu = \frac{1}{\omega}$, it follows that

$$\mathbf{A}^{-1}\mathbf{B}\mathbf{v} = \mu\mu = \frac{1}{\omega}, \qquad \mathbf{C} = \mathbf{A}^{-1}\mathbf{B}, \qquad \mathbf{C}\mu = \frac{1}{\omega} = \mu\mu = \frac{1}{\omega}. \tag{22}$$

This transformation converts the original generalized eigenvalue problem into a standard eigenvalue problem that is accurate near the origin. Then, a small subset (compared with the leading dimension of $\mathbf{A}$ and $\mathbf{B}$) of eigenvalues (equal to the Krylov subspace dimension) m is sought, see [17] for further details.

Because of the shift-invert strategy followed, when applying the Arnoldi algorithm, a number of m non-symmetric linear systems $\mathbf{Cv} = \mathbf{A}^{-1}\mathbf{Bv} = \mathbf{w}$ or, equivalently, $\mathbf{Aw} = \mathbf{Bv}$ must be solved at each iteration, being $\mathbf{w}$ and $\mathbf{v}$ a unknown and known vectors, respectively. The matrix $\mathbf{A}$ is badly conditioned, because of the stiffness associated to the underlying compressible and turbulent NS equation system, and requires the presence of a very low residual incomplete LU pre-conditioner. To avoid the computation of several incomplete LU decompositions until the required convergence of the iterative solvers is obtained, a different strategy is followed. A full LU factorization is performed for the Jacobian matrix $\mathbf{A}$. This strategy, used here in a compressible finite volume context, has also been followed in Biglobal computations of incompressible flows in finite elements discretizations [18, 19] and in the context of spectral methods [20, 21]. The full LU decomposition consumes a large amount of RAM memory. To partially alleviate this requirement, we use sparse matrix format and parallel algorithms. Hence, the solution of these large linear systems for a sparse real non-symmetric matrix $\mathbf{A}$ is calculated using a direct LU factorization performed in parallel by the library MUMPS [22]. A typical leading dimension of the matrix $\mathbf{A}$ used in 2D turbulent problems is $dim(\mathbf{A}) = 3 \times 10^5$, whereas only the nonzero elements of this matrix, $nnz(\mathbf{A}) = 2 \times 10^7$, and those of its LU factorization, 3×10^8, are stored. These numbers increase drastically when a 3D analysis is performed. The leading dimension for our 3D matrix $\mathbf{A}$ is $dim(\mathbf{A}) = 2 \times 10^6$ of which $nnz(\mathbf{A}) = 3 \times 10^8$ are nonzero elements. The corresponding 3D LU factorization requires 9×10^9 nonzeros and 1.2 Tbytes of RAM memory.

The total time needed for a complete global analysis depends on the time necessary to complete the LU factorization, which in terms of CPU time is much higher than required by the Arnoldi iteration process.

3.2. Adjoint problem

In the previous section, the discrete approach has been used to obtain the direct modes of system, and is now extended to calculate its adjoint counterparts. A comparison of the direct and discrete approaches to compute direct and adjoint modes can be found in the recent work by Chandler *et al.* [23]. Regarding adjoint methods for hydrodynamic stability, an overview of recent developments has been compiled by Luchini and Bottaro [24].

In the present work and to the authors' knowledge, adjoint modes associated to the buffet onset have been computed for the first time. In addition, the regions where the direct and adjoint modes overlap define the structural sensitivity to local feedback [25]. These regions are also extracted for this challenging case. The associated sensitivity map provides information on the flow regions where a small localized perturbation causes the largest drift in the eigenvalues and hence provides useful information on control strategies to attenuate these instabilities [24].

To obtain the adjoint discrete operator, associated to the direct matrix $\mathbf{A}$ (defined through Equation (19)), we define the following discrete inner product:

$$< \mathbf{a}, \mathbf{b} >= \mathbf{b}^H \mathbf{B} \mathbf{a}, \tag{23}$$

where $\mathbf{a}$ and $\mathbf{b}$ are the two arbitrary vectors and the superindex H denotes the Hermitian (i.e., the transconjugate). In addition, matrix $\mathbf{B}$ denotes the matrix of volumes that previously appeared in Equation (19) and is associated to the selected finite volume spatial discretization.

Having selected an inner product, the formulation for the discrete adjoint matrix $\mathbf{A}_{Adj}$ can be obtained through the definition of the adjoint operator

$$< \mathbf{a}, \mathbf{Ab} >=< \mathbf{A}_{Adj}\mathbf{a}, \mathbf{b} > . \tag{24}$$

Making use of the definition for the inner product of Equation (23) and manipulating Equation (24), we obtain

$$(\mathbf{Ab})^H \mathbf{Ba} = (\mathbf{b})^H \mathbf{B} \mathbf{A}_{Adj} \mathbf{a}, \tag{25}$$

$$\mathbf{b}^H \mathbf{A}^H \mathbf{Ba} = \mathbf{b}^H \mathbf{B} \mathbf{A}_{Adj} \mathbf{a}. \tag{26}$$

Rearranging the last equation reveals the expression for the discrete adjoint matrix

$$\mathbf{A}_{Adj} = \mathbf{B}^{-1} \mathbf{A}^H \mathbf{B}. \tag{27}$$

The adjoint modes can now be obtained by solving an eigenvalue system; as previously shown for the direct system in Equation (19), we obtain

$$\mathbf{A}_{Adj}\mathbf{q}_{Adj} = \omega_{Adj}\mathbf{B}\mathbf{q}_{Adj}, \tag{28}$$

where ω_{Adj} and $\mathbf{q}_{Adj}$ denote the adjoint eigenvalues and eigenvectors (i.e., adjoint eigenmodes), respectively.

Finally, from a computational point of view, it results more efficient to define a new vector $\bar{\bar{\mathbf{q}}}_{Adj} = \mathbf{B}\mathbf{q}_{Adj}$ such that the eigenvalue system, defined in equation (28), can be rewritten as

$$\mathbf{A}^H\bar{\bar{\mathbf{q}}}_{Adj} = \omega_{Adj}\mathbf{B}\bar{\bar{\mathbf{q}}}_{Adj}. \tag{29}$$

We note that for the particular case of $\mathbf{A}$ being a real matrix (e.g., the finite volume discretization described in this work), we obtain $\mathbf{A}^H = \mathbf{A}^T$. In order to compare the last expression, Equation (29), to the original direct eigenvalue system, Equation (19) (i.e., $\mathbf{A}\mathbf{q} = \omega\mathbf{B}\mathbf{q}$), we can apply the Hermitian operator (resp. the transpose if real matrices are considered) to Equation (29) and obtain

$$\bar{\bar{\mathbf{q}}}^H_{Adj}\mathbf{A} = \omega^H_{Adj}\bar{\bar{\mathbf{q}}}^H_{Adj}\mathbf{B}, \tag{30}$$

where we have assumed that $\mathbf{B}^H = \mathbf{B}$, which is verified for our real diagonal matrix of cell volumes.

This last expression shows that the adjoint eigenvalues ω_{Adj} are the complex conjugate eigenvalues of the original direct eigenvalue system and that the adjoint modes are the left eigenvectors of the original direct matrix $\mathbf{A}$. It can therefore be concluded that only the direct eigenvalue problem needs to be computed because its solution provides both direct and adjoint modes through the right and left eigenvectors of the system, respectively.

Alternatively, one can compute the right eigenvectors of the matrix $\mathbf{A}$ to obtain the direct modes and transpose the matrix to calculate the adjoint modes, which are provided by the right eigenvector of the transpose operator, as shown in Equation (29). If the latter technique is used, the resulting adjoint eigenmodes need to be scaled using the matrix of volumes such that $\mathbf{q}_{Adj} = \mathbf{B}^{-1}\bar{\bar{\mathbf{q}}}_{Adj}$.

The presented computations use the latter technique because the Arnoldi method, which is used to extract the spectral information, does not require modifications (i.e., only right eigenvalues are computed) to compute direct and adjoint modes.

4. RESULTS

Sections 2 and 3 present the linearized forms of the direct and adjoint stability problems. The solution of these eigenvalue problems provides a general framework for the prediction of the onset of flow unsteadiness and the detection of the structural sensitivity (see Section 4.3) areas for compressible and high Reynolds number flows. In this section, the transonic buffet onset for a turbulent NACA0012 airfoil is considered. The results obtained for the direct problem have been compared with previous authors and experiments, whereas the original results coming from the adjoint formulation have been used to detect most sensitive areas. A 3D extrusion of the 2D geometry has also been considered to validate the former results and to confirm the two-dimensionality of the most unstable mode for this geometry. To validate the methodology, results for the vortex shedding for a circular cylinder under laminar flow condition are also included.

4.1. Typical benchmark: vortex shedding for a circular cylinder

The first onset of instability that can be studied at low Reynolds numbers for a circular cylinder encompasses the Hopf bifurcation that leads to a 2D unsteady vortex shedding. This global instability problem has already been studied by different authors [26, 27] and is one of the first problems where the concepts of global stability analysis were applied. Unstable modes, localized at the cylinder wake, are able to break flow symmetry once the Reynolds number surpasses the critical value $Re_{cr} \approx 47$. In order to compare these results with the incompressible case, a low Mach number $M = 0.2$ is used.

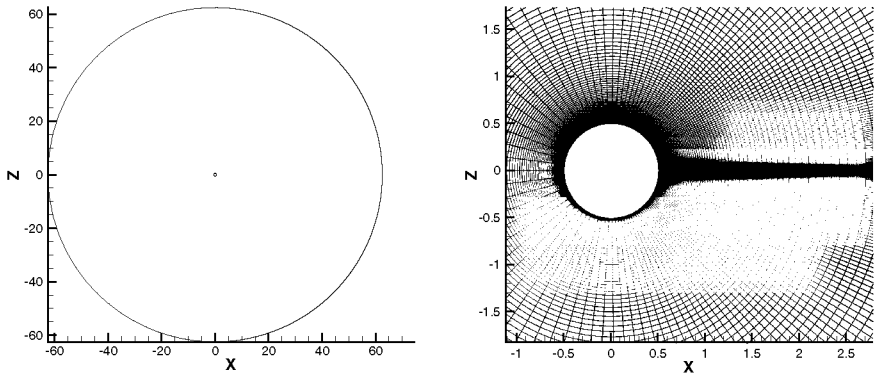

Figure 1. Computational domain(left) and detailed view of the mesh (right) used for the baseflow and the global analysis of the circular cylinder case.

The non-dimensional circular cylinder, with a diameter of $d = 1$ is immersed in a circular domain with a radius of $R/d = 60$ placed in the plane X–Z, see Figure 1. Far-field boundary conditions and no-slip boundary conditions at cylinder walls are selected. Different domain sizes were tested until convergence of the most unstable physical eigenvalues was reached. After a mesh convergence process with iterative refinements, the details of which are not included in this paper, a final mesh with 36,000 quadrilateral elements (36,240 nodes) was selected, see Figure 1. The figure also shows the mesh refinement close to the cylinder wake. Two Reynolds numbers above and below the critical Reynolds number Re_{cr} were computed. The baseflow velocity components (U, W) for a Reynolds number $Re = 60$ based on the cylinder diameter are plotted in Figure 2. According to the stability theory, when the Reynolds number is subcritical, the flow is stable with respect to small unsteady perturbations, whereas the onset of vortex shedding appears when this number surpasses the critical value, breaking the steadiness in the flow. The TAU code [15] when the steady version is selected is able to force this final artificial steady state with a residual tolerance of 10^{-8}. Once the subcritical $Re = 45$ and supercritical $Re = 60$ baseflows are computed and their respective Jacobians obtained, the Arnoldi algorithm is applied to both cases. As can be observed in Table I, when $M = 0.2$ and $Re = 45 < Re_{cr}$, the imaginary part of the eigenvalue is negative, meaning that the baseflow is stable. When the Reynolds number is increased $Re = 60 > Re_{cr}$, the imaginary part of the eigenvalue changes its sign, becoming positive and showing that the corresponding baseflow contains a growing instability leading to an unsteady flow regime.

The calculated spectrum obtained from the solution of the eigenvalue problem expressed by Equation (19) is shown in Figure 3 for $Re = 60$ and $M = 0.2$, where unstable modes appear with a positive imaginary part $\omega_i > 0$. Because of the complexity of the numerical computation of the eigenvalue problem, some spurious modes may appear. In our case, see Figure 3, two unstable

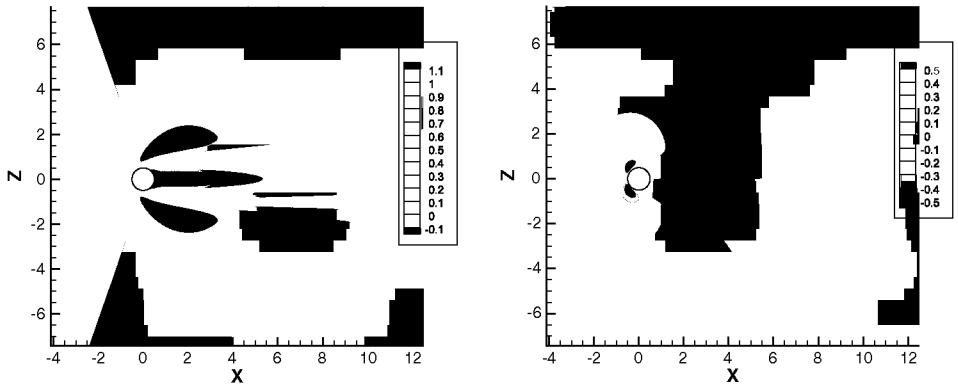

Figure 2. Baseflow mean velocity components U(left) and W(right) for the circular cylinder at $Re = 60$ and $M = 0.2$.

Table I. Most unstable eigenvalues for the subcritical $Re = 45$ and supercritical $Re = 60$ cases.

Re	(ω_r, ω_i)	Reference value (ω_r, ω_i) [8]
45	(0.724, −0.01)	(0.725, −0.01)
60	(0.7332, 0.0427)	(0.7383, 0.0439)

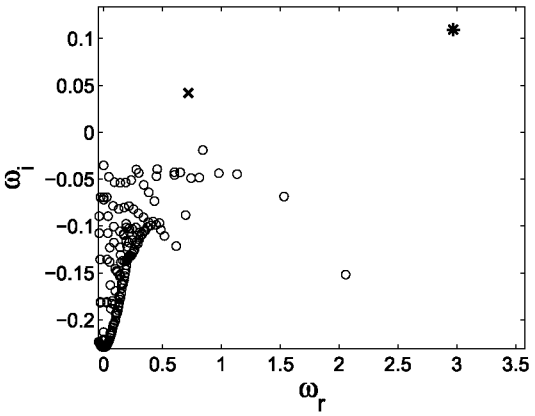

Figure 3. Spectrum for the circular cylinder case at $Re = 60$ and $M = 0.2$. Spurious unstable eigenvalue (*) and real unstable eigenvalue(**x**).

eigenvalues can be seen in the positive imaginary part of the complex plane. There are several criteria to distinguish between real modes and spurious ones: first, the frequency corresponding to the real modes is far from the vortex shedding phenomenon given by the Strouhal number; second, the shape of the eigenvector contains values that are far from the cylinder wake (area where the flow breaks its stability); third, the displacement in the complex plane of the eigenvalue position corresponding to a spurious mode is significantly larger than the real eigenvalues when the spectrum is recomputed with a refined mesh or when the Krylov subspace dimension m is increased. All these criteria are made possible to ensure that the only physical mode of the two unstable ones is the one marked with a cross **x** in the figure, whereas the point marked with an asterisk $*$ is clearly spurious. As shown in Table I, the most unstable values agree well with published results [8], where a compressible approach was also used. In addition, let us note that these tabulated results agree well with other experimental and computational works that assumed the incompressibility of the flow [27–29]. The frequency obtained at $M = 0.2$, $Re = 45$, and $\omega_r = 0.7332$ corresponds to a Strouhal number of $St = 0.1167$, which also matches very well with previous works, see [8, 29]. The momentum perturbation amplitudes corresponding to the real part of the most unstable mode for $M = 0.2$ and $Re = 60$ are shown in Figure 4. This image shows the modal pattern of the vortex shedding process (i.e., von Karman street). This first benchmark shows how global stability is able to predict the onset of vortex shedding when applied to a laminar flow with low compressibility effects.

4.2. Case 1: Transonic buffet in a 2D NACA0012 profile

Here, we consider the onset of unsteadiness for a transonic NACA0012 airfoil. In contrast with the previous benchmark, the Reynolds number based on the chord is high $Re = 10^7$ and the Mach number is large $M = 0.76$, meaning that turbulent and compressible effects must be considered. In contrast to the previous laminar case, a new field $\tilde{\nu}$ representing turbulent effects is added to both the baseflow $\mathbf{Q}$ and the perturbation $\widetilde{\mathbf{q}}$ vectors. It is well known, see [2, 4, 5], that the complex physics present at the suction side of the airfoil are characterized by a strong shock boundary layer interaction leading to flow separation, see [30]. Depending on the angle of attack α, the interaction of both phenomena could make the flow globally unstable leading to the buffet onset. This instability occurs when α exceeds some critical value which depends on the Reynolds and Mach numbers. In

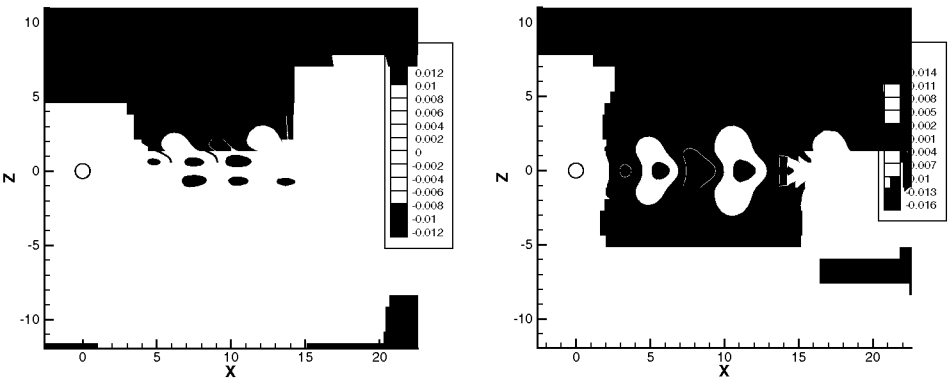

Figure 4. Amplitude of the perturbed momentum components $\widehat{\rho u}$ (left) and $\widehat{\rho v}$ (right) for $Re = 60$ and $M = 0.2$.

those supercritical circumstances, the separation bubble grows and reduces the effective camber of the airfoil, shifting the shock upstream where the pre-shock Mach number is reduced and the shock loses strength. The shock boundary layer interaction is weakened, and the flow reattaches followed by a shock motion downstream where the shock gains strength again. The feedback loop is closed and the cycle continues.

The computational domain designed for this case requires a circular domain placed on the X–Z plane, with the NACA0012 profile set in the center. The non-dimensional NACA0012 airfoil with chord c is immersed in a circular domain with radius $R = 100$ c. Different domain sizes were tested until convergence of the most unstable physical eigenvalues. Far-field boundary conditions were used for the external boundary and no-slip boundary conditions for the airfoil. Several grids were used to study the buffet onset, some of them completely structured whereas others were hybrid (quadrilateral elements close to the NACA profile and the shock wave refinements and triangles for the rest of the computational domain), see Figure 5. After a systematic grid convergence process, a final hybrid mesh was designed to solve both the baseflow and the direct and adjoint stability problems. This selected mesh contains a local refinement around the boundary layer with chordwise and normal spacings of $(dx_{bl}, dz_{bl}) = (8 \times 10^{-3}, 10^{-6})$. The shock wave region with size area $(dx_{sw}, dz_{sw}) = (0.2, 0.24)$ presents an initial unstructured part of size 3×10^{-3} that decreases to 6×10^{-4} where it is connected with the boundary layer refinement with size $(dx_{bls}, dz_{bls}) = (6 \times 10^{-4}, 6 \times 10^{-7})$.

Figures 6–8 show the density, pressure, horizontal velocity component, Mach number, and eddy viscosity fields of the converged steady-state solution at $Re = 10^7$, $M = 0.76$, and $\alpha = 3.2°$. To obtain this solution, the steady version of the TAU code was run until the maximum residual in all variables contained in $\mathbf{Q}$ was less than 10^{-8}. It can be observed in the figures that the shock wave

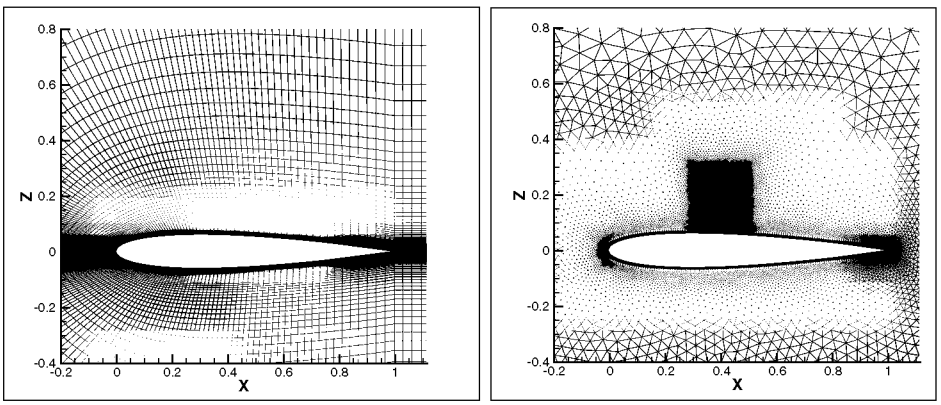

Figure 5. Structured(left) and hybrid(right) mesh designs for the NACA0012 geometry.

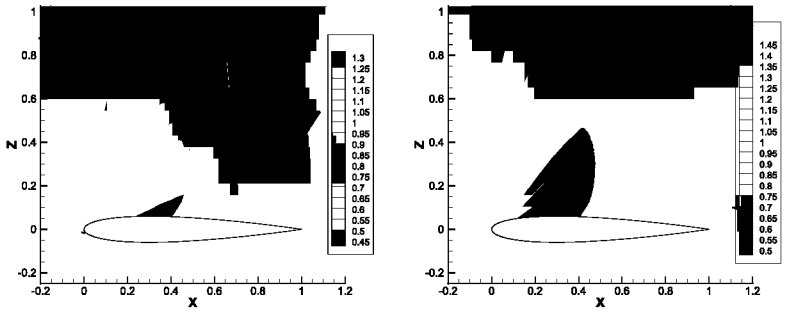

Figure 6. Density (left) and pressure (right) contour fills for the steady baseflow at $Re = 10^7$, $M = 0.76$, and $\alpha = 3.2$.

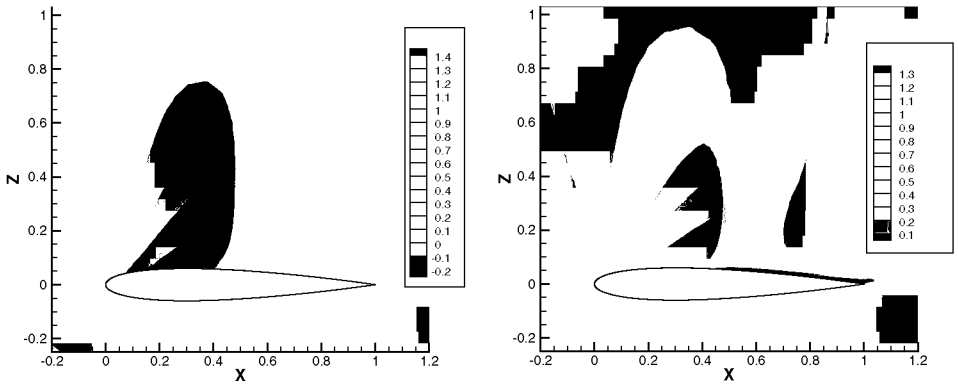

Figure 7. Horizontal velocity component (left) and Mach number (right) contour fills for the steady baseflow at $Re = 10^7$, $M = 0.76$, and $\alpha = 3.2$.

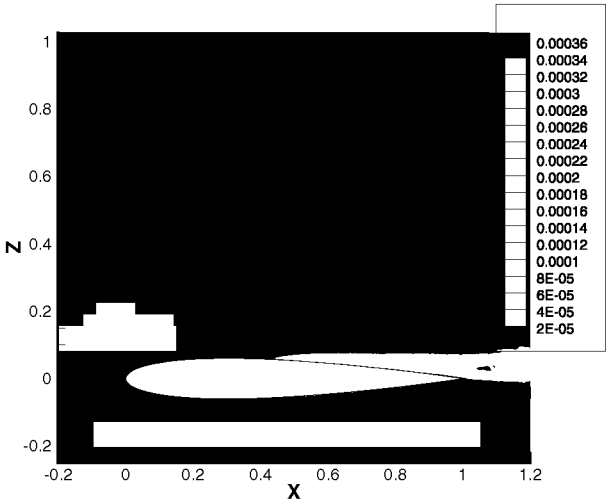

Figure 8. Eddy viscosity contour fills for the steady baseflow at $Re = 10^7$, $M = 0.76$, and $\alpha = 3.2$.

appears at $x/c = 0.45$. It is also relevant to indicate that the number of grid points necessary to capture the shock is 3. This shock has not been artificially smoothed to obtain this solution.

4.2.1. Stability analysis results. The baseflow detailed in Section 4.2 is used for the construction of the eigenvalue problem and the resulting spectrum plotted in the left part of Figure 9. As for the cylinder case, a spurious eigenvalue with positive imaginary part $(\omega_r, \omega_i) = (2.4848, 0.4021)$

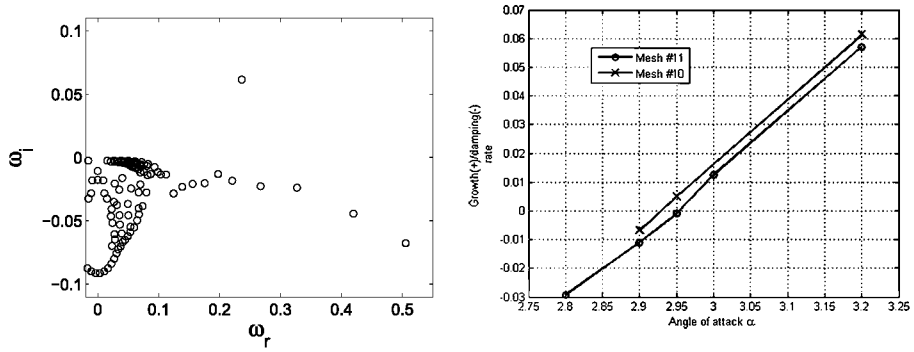

Figure 9. Left: spectrum solution of the eigenvalue problem at $Re = 10^7$, $M = 0.76$, and $\alpha = 3.2$. Right: growth and damping rates for $Re = 10^7$ and $M = 0.76$ for different angles of attack for the NACA0012.

Table II. Most unstable eigenvalues for different hybrid mesh designs for the NACA0012 at $Re = 10^7$, $M = 0.76$, and $\alpha = 3.2°$. Reference value $(\omega_r, \omega_i) = (0.285, 0.045)$ [8].

Number of nodes	ω_r	ω_i
39,629	0.2073	1.04e-1
40,112	0.2386	8.16e-2
46,275	0.2413	4.07e-2
52,982	0.2065	9.95e-2
58,537	0.2369	6.14e-2
60,201	0.2382	5.70e-2
69,800	0.2381	5.57e-2

is found but discarded as a physical instability. A mesh convergence process has been followed in order to detect the quantitative value of the physical unstable eigenvalue, see Table II. The evolution of the imaginary part of the eigenvalue ω_i, when the angle of attack is increased, can be observed for two different meshes in Figure 9. According to this figure, the critical angle of attack is around $\alpha_c = 2.93°$ for the mentioned Reynolds and Mach numbers. A frequency around $\omega_r = 0.27$ for the physical unstable eigenvalue predicted at $Re = 10^7$, $M = 0.76$, and $\alpha = 3.2°$ can also be estimated. This frequency represents the oscillations of the shock wave and shear layer positions as detailed at the beginning of Section 4.2.

In these type of problems, two time scales can be distinguished. On the one hand, the turbulent time scale dominates the viscous shear layer zone and is associated to a high frequency phenomenon. The turbulence closure model used for the base flow computation and also for the linearized eigenvalue problem averages over time these high frequency effects and provides a mean flow and a Jacobian that include this physical turbulence as an average. On the other hand, the low frequency buffet time scale is simulated and presents the aim of our stability analysis. The wide gap between these two time scales provides the possibility of solving one scale while modeling the other. As commented by Crouch in [8], the importance of the turbulence model is crucial for the instability prediction. Other turbulence models, such as Menter's Shear Stress Transport (SST) and $k-\omega$ or even the same S–A turbulence model but without the compressibility term (see Appendix for details), are unable to predict unstable modes for the present flow conditions. Prior to the onset of global instability, the computed turbulence averaged baseflow is the true mean flow (to within the approximation of the turbulence model). Regarding the buffet time scale, let us note that turbulence is only important for its effects on the mean flow. This is, in fact, the classical distinction between turbulence and unsteadiness, see [9] for further details.

The real part of the horizontal $\widehat{\rho u}$ and vertical $\widehat{\rho v}$ momentum and the energy $\widehat{\rho E}$ and the turbulent viscosity $\widehat{\rho\tilde{\nu}}$ perturbation amplitudes are shown in Figures 10 and 11 for $Re = 10^7$, $M = 0.76$, and $\alpha = 3.2°$. It can clearly be seen how the mode is confined close to the shock region and also in the downstream region of the boundary layer (specially for the turbulent viscosity perturbation

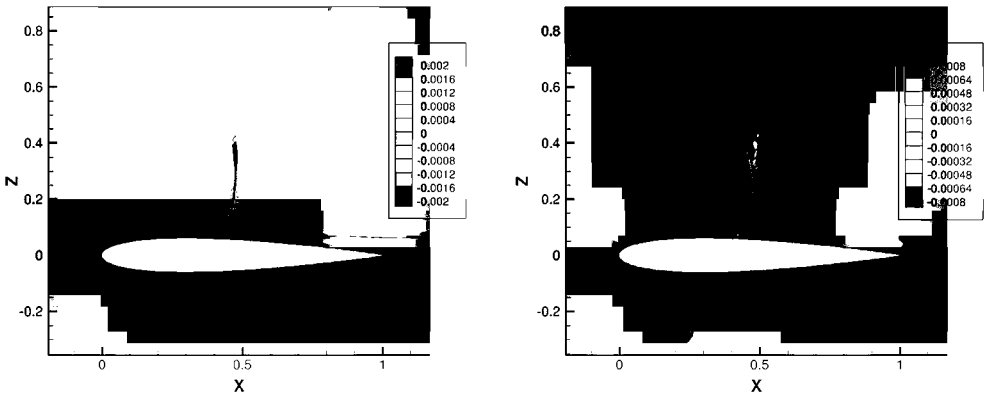

Figure 10. Horizontal (left) and vertical (right) momentum perturbation amplitude corresponding to the physical unstable mode for the NACA0012 at $Re = 10^7$, $M = 0.76$, and $\alpha = 3.2$.

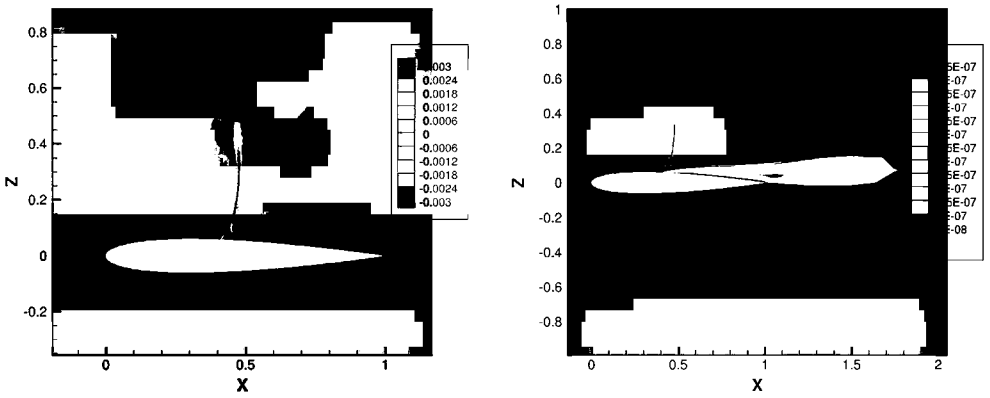

Figure 11. $\widehat{\rho E}$ (left) and $\widehat{\rho \tilde{\nu}}$ (right) perturbation amplitudes corresponding to the physical unstable mode for the NACA0012 at $Re = 10^7$, $M = 0.76$, and $\alpha = 3.2$.

amplitude). In contrast to what other authors indicate about the possibility of containing some 'ringing' in the neighborhood of the shock for the most unstable eigenvector solution, see [8]. Figures 10 and 11 show that the linear perturbation does not contain any 'ringing' close to the shock, and consequently, no smoothing has been found necessary in our computations. An interesting discussion about the dependance of the eigenvalues on the mesh size near the shock wave area and the shock smoothing process can be found in [8], where it is confirmed that neither the prediction of the stability boundaries nor the frequency are strongly influenced (less than 0.03 % in the critical angle of attack and less 4% in frequency). Our predictions at $Re = 10^7$ for different Mach numbers have been compared with previous authors [8] and experimental results of McDevitt and Okuno [2], see Figure 12, where the critical angle of the aforementioned attack which the buffet onset has been compared. The results agree very well with the previous published data. Finally, note that when the Mach number is above certain limit, the critical angle of attack is over-predicted as was noted previously [8]. The causes of these differences are, to date, unclear.

4.3. Adjoint analysis and control of the 2D NACA0012 profile under buffeting conditions

This section includes results for the adjoint mode associated to the most unstable direct eigenmode, calculated using the discrete adjoint methodology detailed in Section 3.2. The real parts of the adjoint eigenmode, corresponding to the $\widehat{\rho u}$ and $\widehat{\rho w}$ components, are shown in Figure 13 ($\widehat{\rho u}$, left and $\widehat{\rho w}$, right). It can be seen that the adjoint mode presents a shock wave-like shape traveling upstream from the intersection between shock and separated flow. This upstreamed adjoint shock can be explained by the upstreaming advective nature of the adjoint equations [24]. In addition,

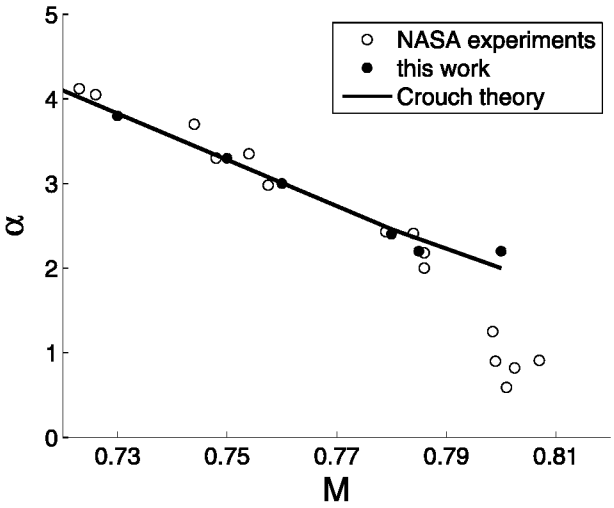

Figure 12. Stability curve α versus Mach number for the NACA0012 airfoil at $Re = 10^7$. Experimental results from [2] and computational results from [8].

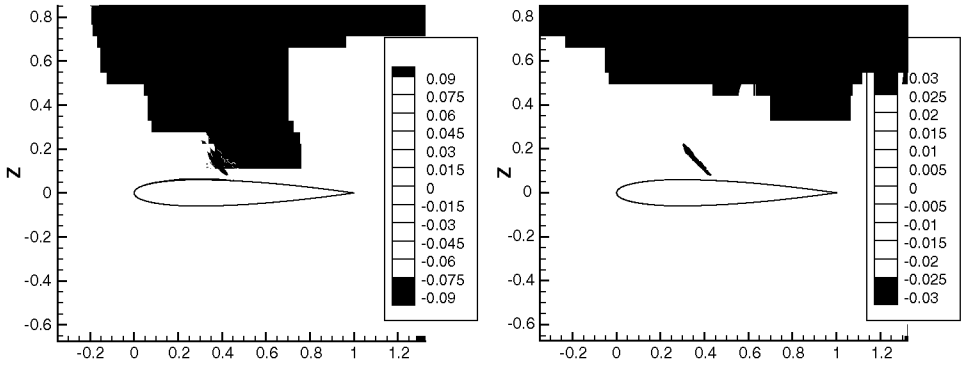

Figure 13. Horizontal and vertical momentum components of the most unstable mode of the adjoint formulation. Left: horizontal. Right: vertical.

the adjoint mode provides information about the flow receptivity to external forcing, and hence, the upstream nature of the mode indicates that the regions were an external force (i.e., momentum source) that would be more influential and therefore its upstreaming nature is not surprising.

Comparing the adjoint mode, Figure 13, to the direct mode, Figure 10, it can be seen that the x-momentum component presents minimum overlap. To quantify this overlap, the structural sensitivity [23, 25] is computed, thus locating the most sensitive regions of the eigenvalue problem to localized feedback (internal changes in the system or wavemaker region). The structural sensitivity maps can be calculated using the expression $S = ||\mathbf{q_{Adj}}|| \cdot ||\hat{\mathbf{q}}||$ with $< \mathbf{q_{Adj}}, \hat{\mathbf{q}} >= 1$, with $\hat{\mathbf{q}}$ and $\mathbf{q_{Adj}}$ as the direct and adjoint modes, where $< \bullet, \bullet >$ denote the inner product defined by Equation (23) in Section 3.2, with its associated norm $||\bullet|| = < \bullet, \bullet >^{1/2}$. The resulting sensitivity map for the NACA0012 is shown in Figure 14. The localized region of sensitivity denotes the wide spatial separation between direct and adjoint modes, which is related to the non-normality [31] of the compressible and turbulent Navier–Stokes equations. Finally, the sensitivity region shows that flow modifications leading to a more stable system (i.e., flow control strategies) should be introduced in the junction between the shock wave and the separated flow. Indeed, the core region of the instability, the wavemaker region, is located at the intersection of these two physical phenomena. This analysis confirms that the origin of the instabilities causing the buffeting phenomenon is located at the interaction between the shock and the detached boundary layer.

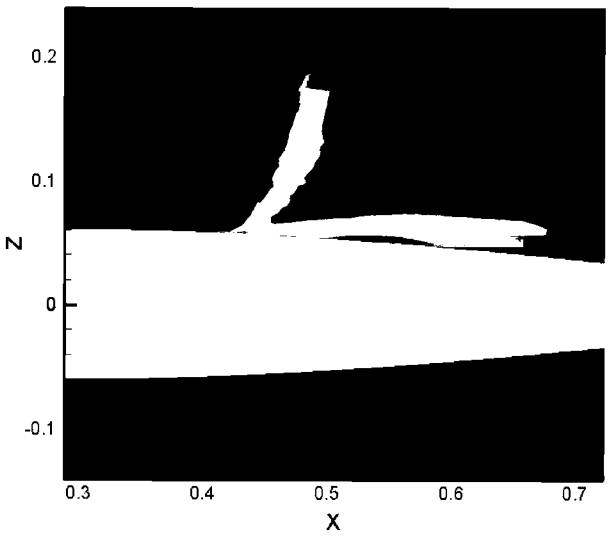

Figure 14. Sensitivity region.

Regarding the convergence of the adjoint mode, let us clarify that in this work, the adjoint modes are obtained through the discrete approach, see Section 3.2. This approach makes use of a purely algebraic manipulation of the Jacobian matrix A (and mass matrix B) to extract the adjoint mode associated to the most unstable direct mode. Because we have ensured that the direct mode is converged (by performing a grid independence study), we are implicitly ensuring that the corresponding adjoint mode is also converged (i.e., both modes have eigenvalues that are exactly complex conjugate of each other). In other words, if the discretization of the Jacobian and mass matrix is good enough for the direct mode, it is also good for the discrete adjoint (we cannot do better). An alternative viewpoint is provided by the physical interpretation of the adjoint mode. The adjoint provides information of the receptivity of the direct mode to changes in the flow such as mesh variation or grid refinement. When refining the grid to capture the direct mode, we have implicitly refined the region where the adjoint mode lies up to the point where the adjoint region is refined enough to not affect the direct mode. The refinement of the direct calculation has therefore indirectly ensured that the adjoint is converged.

4.4. Case 2: 3D stability analysis of the NACA0012 profile at buffet conditions

As in many other flows in turbulent regime, the possibility of having 3D structures that could alter the 2D prediction should be considered. In order to study this possibility, a 3D extruded version of the 2D NACA0012 in the Y-direction has been created. A 3D steady baseflow is calculated and a stability analysis is performed for the same Reynolds and Mach numbers as selected for the 2D case. The aim of this study is to answer whether the Triglobal linear stability theory predicts the same mode computed under the 2D assumptions or whether the presence of spanwise flow variations alters the buffet onset phenomenon. The main idea is to explore the spectrum changes when the three velocity components are allowed to vary in the extruded geometry.

In this 3D case, the computational domain is a cylinder with radius $R = 100c$ that has been constructed extruding the 2D geometry and L_y being the extrusion length. Different spanwise lengths $L_y = c, 2c, 4c$ have been considered. Similar to the 2D case, far-field boundary conditions are used for the external boundary and a no-slip boundary conditions for the airfoil are used. On the lateral planes, symmetric boundary conditions are imposed. For this 3D case, an extruded mesh based on the hybrid 2D mesh used in Section 4.2 has been created.

An important issue is to compare the steady-state solution for the 2D and 3D simulations, where for the former, no velocity component or gradients were permitted in the spanwise direction. The flow fields density, pressure, velocity components, Mach number, and turbulent viscosity have been

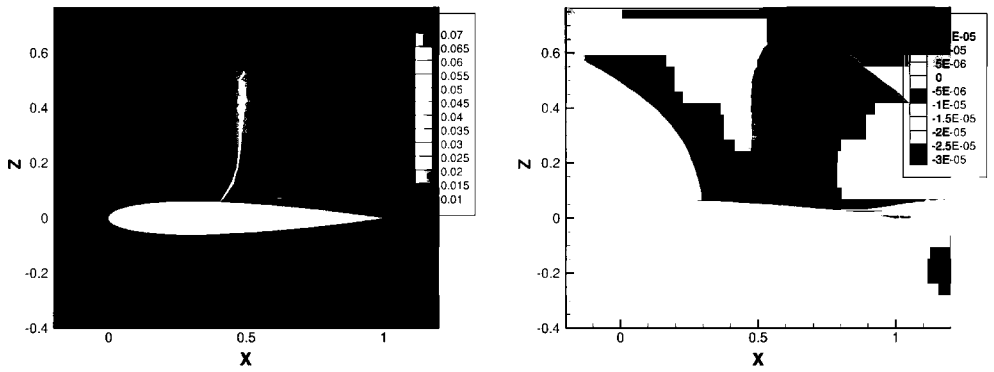

Figure 15. Density (left) and spanwise velocity (right) difference between the 3D and 2D baseflows at $Re = 10^7$, $M = 0.76$, and $\alpha = 3.2$.

Table III. Computational details of the two largest 3D stability analysis computations.

L_y	Number of nodes	Leading dimension	Number of non-zero elements	Memory consumption (Gb)
$2c$	175,611	10^6	1.5×10^8	754
$4c$	292,685	1.7×10^6	3×10^8	1766

compared assuming identical maximum residuals when reaching the steady-state stopping criteria. The maximum local difference between the 2D and 3D converged steady-state solutions has been found for the density scalar field, around 7%, see Figure 15. The spanwise velocity difference is also presented in Figure 15, where it can be seen that this component is several orders of magnitude smaller than the other two components. This effect is even more significant in terms of velocity gradients (not shown). It has been observed that the shock wave appears at the same position $x/c = 0.45$. As for the 2D case, no smoothing process has been done in the shock region. The source of the differences between the 2D and the 3D flow fields results from the fact that the three velocity components are allowed to vary in the 3D simulation.

These differences shown in Figure 15 between the 2D and 3D cases, which open the discussion about the possible variation of the stability analysis when a spanwise component is allowed. Consequently, a Triglobal analysis is required in order to confirm if the 2D results are still valid or if the buffet onset could be altered and a new unstable mode appears.

The future objective of this research is to analyze a 3D wing geometry where the chord length varies along the spanwise direction (i.e., tapered wing), and consequently, the geometry is not homogeneous in the spanwise direction making difficult the application of a Biglobal approach. The case presented here is a preliminary approximation to the mentioned future objective. In addition, this Triglobal calculation provides some guidelines in terms of memory requirements to perform a computation of industrial relevance.

4.4.1. Triglobal stability analysis results. It is worth mentioning that to the authors' knowledge, this computation is the first Triglobal analysis performed for a compressible turbulent 3D flow in the presence of a shock wave. Computational details of the two largest cases are summarized in Table III. Note the large memory consumption due to the necessity of performing an LU decomposition of the 3D Jacobian matrix. Other alternatives, different to direct LU decomposition, were tried but no convergence was obtained for the linear systems involved in the Arnoldi algorithm. According to our experience, the ill conditioning of the Jacobian matrix is due to complexity (i.e., system stiffness) given by the combination of turbulence and the presence of shock waves. As observed in the 2D case, the mesh refinement in the shock wave region has a significant influence on the numerical values of the spectrum. In the left part of Figure 16, the eigenvalues corresponding to a mesh with and without refinement are compared. Because of the presence of a large number of

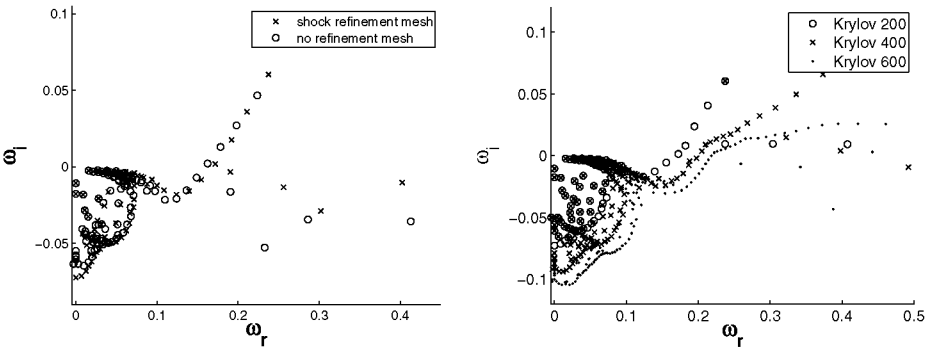

Figure 16. Left: comparison between the spectrum computed with a mesh where the shock wave region was refined and another mesh without refinement. Right: convergence process using the Krylov subspace dimension as parameter.

spurious unstable modes in this computation, the influence of the Krylov subspace dimension m in the accuracy of the eigenvalues was investigated. In the right part of Figure 16, different spectra corresponding to increasing values of m are shown. It is well known that the increase of the Krylov subspace dimension m implies a reduction of the number of spurious eigenvalues. As can be observed, all the spurious eigenvalues move significantly when the value of m is increased. It is remarkable that when most of the unstable eigenvalues move, the eigenvalue that contains physical relevance remains at the same position, see Figure 16. The presence of velocity in the spanwise direction substantially changes the spurious eigenvalues, whereas the physical unstable eigenvalue remains at the same place of the spectrum, see the left part of Figure 17. When the length of the geometry is changed, the physical eigenvalue representing the buffet phenomenon remains at the same location confirming that the physics of the mode are purely 2D, see Figure 17. The final aspect of the computed eigenvector representing the horizontal momentum perturbation amplitude of the most unstable mode is shown in Figure 18. It can be seen that the mode is very similar to the previous one presented for the 2D case.

An important conclusion is that, although the spectrum is changed by the presence of 3D flow, the relevant physics involved in the buffet onset are constrained to the X–Z plane where the gradients due to the shock wave are more significant than those in the spanwise direction. In this case, and unlike in 2D problems where the onset of a spanwise instability is studied [17], the buffet onset is a complex interaction phenomena (shock wave and detached shear layer) well captured by the 2D flow, as shown in the right part of Figure 17. As suspected, the 3D unstable mode is an extruded version of the 2D mode computed in Section 4.2.1, see Figure 10 where the real part of the horizontal momentum perturbation $\widehat{\rho u}$ is plotted. An interesting conclusion is that although experiments are

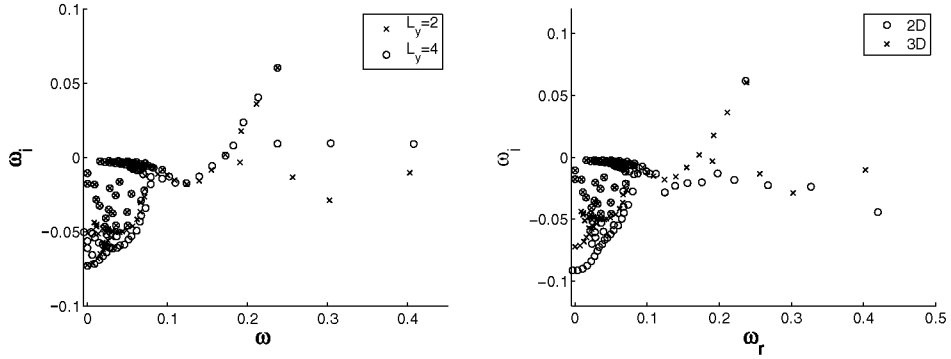

Figure 17. Left: comparison between the spectrum computed using $L_y = 2$ and $L_y = 4$. Right: comparison between the 2D and 3D spectrum computed using $L_y = 4$.

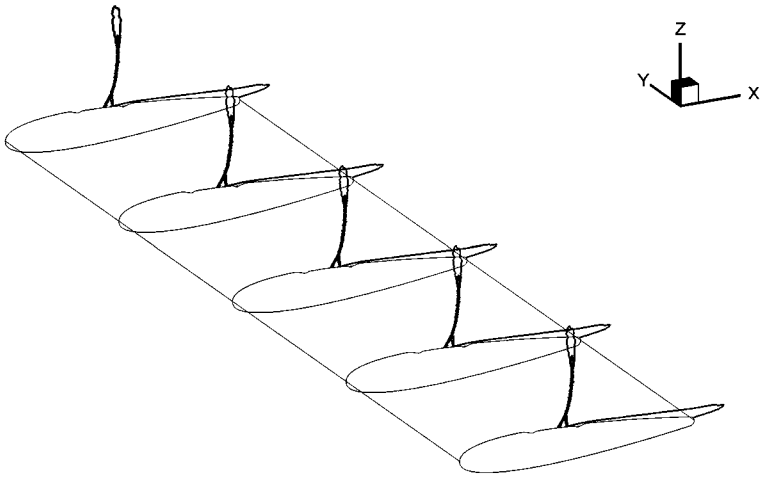

Figure 18. Horizontal momentum perturbation amplitude of the Triglobal unstable mode for the extruded NACA0012 geometry for the referenced conditions. Eleven equispaced contour lines are represented between −0.024 and 0.002 values.

intrinsically 3D [2], the physics represented by just one 2D section are relevant enough for the buffet prediction. The small differences between the 2D and 3D stability analysis results suggest that a 2D analysis is enough to predict the buffet onset.

Finally, small 3D variations in the baseflow do not seem to perturb the position of the 2D most unstable eigenmode for the buffet phenomenon. This underlines the importance of the buffet phenomenon in the context of real engineering applications, where noise levels are present in all the 3D flow field components.

5. CONCLUSIONS

In this paper, the following conclusions have been addressed:

1. A numerical analysis based on a finite volume discretization of the compressible version of the Navier–Stokes equations and a subsequent extraction of the linearized Jacobian of the formulation have been allowed for the prediction of the Hopf instability onset for different flows.
2. This methodology can be applied to a wide variety of flows including weakly or significantly compressible flows where shock waves are present, in either laminar or turbulent regimes.
3. Global stability analysis is an accurate numerical tool to detect and predict instabilities leading to unsteady perturbations.
4. Results and experiments for the problems considered in this work are in good agreement with the previous literature.
5. The turbulence model used and the mesh refinements have quantitative effects on the buffet onset prediction.
6. A forced steady-state baseflow, which is in fact an average flow (using RANS type turbulence models), can be used for the linearized formulation when the searched frequencies are far enough from the turbulent frequencies.
7. The method has been extended to the discrete adjoint formulation, and a sensitivity map has been obtained. The wavemaker region has been shown to be located where the shock wave interacts with the detached boundary layer.
8. An extended 3D version using an extruded mesh has also been computed for the NACA0012 geometry confirming that, in this case, the buffet onset is of a purely 2D nature.

APPENDIX: SPALART–ALMARAS IMPLEMENTATION

The turbulence transport equation could be written in the following way:

$$\frac{\partial \rho \tilde{\nu}}{\partial t} + \frac{\partial \rho u_i \tilde{\nu}}{\partial x_i} = P + \left[\frac{\partial}{\partial x_i} \left(\frac{\mu_l + \tilde{\mu}}{\sigma} \frac{\partial \tilde{\nu}}{\partial x_i} \right) + \rho \frac{c_{b2}}{\sigma} \left(\frac{\partial \tilde{\nu}}{\partial x_i} \right)^2 \right] - D, \tag{A.1}$$

where the right-hand side of the equation comprises the production, the gradient diffusion, and the wall destruction of the turbulent kinematic viscosity. These production and destruction terms could be expressed as

$$P = c_{b1} \rho \tilde{S} \tilde{\nu} \quad , \qquad D = c_{w1} f_w \rho \left(\frac{\tilde{\nu}}{d} \right)^2, \tag{A.2}$$

where d is the wall distance. The other parameters are considered as follows:

$$\mu_t = \rho \nu_t \quad , \qquad \nu_t = f_{v1} \tilde{\nu} \quad , \qquad f_{v1} = \frac{\chi^3}{\chi^3 + c_{v1}^3} \quad , \qquad \chi = \frac{\tilde{\nu}}{\nu_l}. \tag{A.3}$$

ν_l is the laminar kinematic viscosity, whereas ν_t is the turbulent kinematic viscosity. The value of $\tilde{\nu}$ is equal to ν_t everywhere except in the buffer layer where it is modified to take into account the near-wall viscous region.

In the S–A model, the total production of turbulence is related to a modified magnitude of the vorticity.

$$\tilde{S} = |\vec{\omega}| + \frac{\tilde{\nu}}{k^2 d^2} f_{v2} \quad , \qquad \vec{\omega} = \nabla \times \mathbf{v}, \tag{A.4}$$

with

$$f_{v2} = 1 - \frac{\chi}{1 + \chi f_{v1}} \quad , \qquad \chi = \frac{\tilde{\nu}}{\nu_l}, \tag{A.5}$$

$$f_w = g \left(\frac{1 + c_{w3}^6}{g^6 + c_{w3}^6} \right)^{1/6} \quad , \qquad g = r + c_{w2}(r^6 - r) \quad , \qquad r = \frac{\tilde{\nu}}{\tilde{S} k^2 d^2}, \tag{A.6}$$

where f_w is the wall-blockage function and g is the limiter function. Because f_{w2} could be negative, leading to a negative value of $\tilde{S}$, the parameter r is defined as

$$r = \frac{\tilde{\nu}}{MAX\left(\tilde{S}, \epsilon\right) k^2 d^2} \quad , \qquad \epsilon = 10^{-16}. \tag{A.7}$$

In the present work, the S–A turbulence model was used with the compressibility correction as defined in [13], adding the following correction term in the RHS of Equation (A.1)

$$- c_5 \frac{\tilde{\nu}^2}{a^2} \frac{\partial u_i}{\partial x_j}, \tag{A.8}$$

where a is the speed of sound.

The values used for the various constants are reported as follows.

$$c_{b1} = 0.1355 \quad , \qquad \sigma = 2/3 \quad , \qquad c_{b2} = 0.622 \quad , \qquad k = 0.41 \quad , \qquad c_5 = 3.5, \tag{A.9}$$

$$c_{w2} = 0.3 \quad , \qquad c_{w3} = 2 \quad , \qquad c_{v1} = 7.1 \quad , \qquad c_{t3} = 1.2 \quad , \qquad c_{t4} = 0.5, \tag{A.10}$$

$$c_{w1} = \frac{c_{b1}}{k^2} + \frac{1 + c_{b2}}{\sigma}. \tag{A.11}$$

ACKNOWLEDGEMENTS

The research leading to these results has received funding from the European project Advances in Numerical and Analytical tools for DEtached flow prediction (ANADE) under the grant contract PITN-GA 289428.

All the authors would like to thank Mr. Hugo Gee for his valuable assistance during the preparation of this manuscript and Mr. Jorge Posin for the valuable discussions on the contents of this work.

REFERENCES

1. Technical report of the accidents investigation subcommittee on the accident to the aeroplane G.AAZK at Meopham, Kent on 21st July, 1930, *(R&M 1360)*, British Aeronautical Research Committee, London, January 1931.
2. McDevitt JB, Okuno AF. Static and dynamic pressure measurements on a NACA0012 airfoil in the Ames high Reynolds number facility, *NASA Tech. Paper 2485*, National Aeronautics and Space Administration, Scientific and Technical Information Branch, Washington, D.C., 1985.
3. Lee BHK. Oscillatory shock motion caused by transonic shock boundary-layer interaction. *AIAA Journal* 1990; **28**:942–944.
4. Barakos G, Drikakis D. Numerical simulation of transonic buffet flows using various turbulence closures. *International Journal of Heat and Fluid Flow* 2000; **21**:620–626.
5. Chung I, Lee D, Reu T. Prediction of transonic buffet onset for an airfoil with shock induced separation bubble using steady Navier-Stokes solver. *AIAA Paper 2934, 20th AIAA Applied Aerodynamics Conference*, Saint Louis, MO, June 24–26 2002.
6. Brunet V, Deck S, Molton P, Thiery M. A complete experimental and numerical study of the buffet phenomenon over the oat15a airfoil, *40ème Colloque Aérodynamique Appliquée*, Toulouse, France 21-23 March 2005.
7. Theofilis V. Global linear instability. *Annual Review of Fluid Mechanics* 2011; **43**:319–52.
8. Crouch JD, Garbaruk A, Magidov D. Predicting the onset of flow unsteadiness based on global instability. *Journal of Computational Physics* 2007; **224**:924–940.
9. Crouch JD, Garbaruk A, Magidov D, Travin A. Origin of transonic buffet on aerofoils. *Journal of Fluid Mechanics* 2009; **628**:357–369.
10. Garbaruk A, Crouch JD. Quasi-three dimensional analysis of global instabilities: onset of vortex shedding behind a wavy cylinder. *Journal of Fluid Mechanics, Cambridge University Press* 2011; **677**:572–588.
11. Timme S, Badcock KJ, Wu M, Spence A. Lyapunov inverse iteration for stability analysis using computational fluid dynamics. *53rd AIAA/ASME/ASCE/AHS/ASC Structures, Structural Dynamics, and Materials Conference*, Honolulu, Hawaii, 2012; AIAA Paper 2012–1563.
12. Spalart PR, Allmaras SR. A one-equation turbulence model for aerodynamic flows. *La Recherche Aérospatiale* 2000; **1**:5–21.
13. Spalart PR. Trends in turbulence treatments, *AIAA Paper 2000-2306*, American Institute of Aeronautics and Astronautics, Denver, June 19–22 2000.
14. LeVeque RJ. *Finite Volume Methods for Hyperbolic Problems*, Vol. 31 of Cambridge text in Applied Mathematics. Cambridge University Press, 2002.
15. Technical Documentation of the DLR TAU-Code Release 2011.1.0. (Available from: http://tau.dlr.de/startseite/).
16. Anderson JL, Thomas WK, Van Leer B. Comparison of finite volume flux vector splittings for the Euler equations. *AIAA Journal* 1986; **24**(9):1453–1460.
17. González LM, Theofilis V, Gómez-Blanco R. Finite-element numerical methods for viscous incompressible biglobal linear instability analysis on unstructured meshes. *AIAA Journal* April 2007; **45**(4):840–855.
18. Ding Y, Kawahara M. Three-dimensional linear stability analysis of incompressible viscous flow using the finite element method. *International Journal for Numerical Methods in Fluids* 1999; **31**(2):451–479.
19. González LM, Gómez-Blanco R, Theofilis V. Eigenmodes of a counter-rotating vortex dipole. *AIAA Journal* 2008; **46**(11):2796–2805.
20. Theofilis V, Duck PW, Owen J. Viscous linear stability analysis of rectangular duct and cavity flows. *Journal of Fluid Mechanics* 2004; **505**:249–286.
21. González LM, Theofilis V, Sherwin SJ. High-order methods for the numerical solution of the biglobal linear stability eigenvalue problem in complex geometries. *International Journal for Numerical Methods in Fluids* 2011; **65**: 923–952.

22. Amestoy PR, Duff IS, L'Excellent JY, Koster J. A fully asynchronous multifrontal solver using distributed dynamic scheduling. *SIAM Journal of Matrix Analysis and Applications* 2001; **23**(1):15–41.
23. Chandler GJ, Juniper MP, Nichols JW, Schmid PJ. Adjoint algorithms for the Navier–Stokes equations in the low Mach number limit. *Journal of Computational Physics* 2012; **231**(4):1900 –1916.
24. Luchini P, Bottaro A. Adjoint equations in stability analysis. *Annual Review of Fluid Mechanics* 2014; **46**:493–517.
25. Giannetti F, Luchini P. Structural sensitivity of the first instability of the cylinder wake. *Journal of Fluid Mechanics* 2007; **581**:167–197.
26. Williamson CHK. Vortex dynamics in the wake of a cylinder. In *Fluid Vortices*, Green SI (ed.). Kluwer Academic Publishing: Amsterdam, Holland, 1995; 155–234.
27. Barkley D, Henderson RD. Three-dimensional floquet stability analysis of the wake of a circular cylinder. *Journal of Fluid Mechanics* 1996; **322**:215–241.
28. Hammache M, Gharib M. An experimental study of the parallel and oblique vortex shedding from circular cylinders. *Journal of Fluid Mechanics* 1991; **232**:567–590.
29. Jackson CP. A finite-element study of the onset of vortex shedding in flow past variously shaped bodies. *Journal of Fluid Mechanics* 1987; **182**:23–45.
30. Illi S, Krämer E, Lutz T. On the capability of unsteady rans to predict transonic buffet. *Third Symposium Simulation of Wing and Nacelle Stall, June 21st - 22nd*, Braunschweig, Germany, 2012.
31. Chomaz JM. Global instabilities in spatially developing flows: non-normality and nonlinearity. *Annual Review of Fluid Mechanics* 2005; **37**(1):357–392.